Powder Technology 407 (2022) 117622

Contents lists available at ScienceDirect

Powder Technology

journal homepage: www.journals.elsevier.com/powder-technology

Three-dimensional simulation of impinging jet atomization of soft mist inhalers using the hybrid VOF-DPM model

Wen Jin [a,b], Jie Xiao [c,**], Hongxian Ren [a], Changhui Li [b], Qijun Zheng [b], Zhenbo Tong [a,b,*]

[a] School of Energy and Environment, Southeast University, Nanjing 210096, China
[b] Department of Chemical Engineering, Monash University, Clayton, VIC 3800, Australia
[c] School of Chemical and Environmental Engineering, College of Chemistry, Chemical Engineering and Materials Science, Soochow University, Suzhou, 215123, China

HIGHLIGHTS

- Modeling the nozzle system of the Soft Mist Inhalers as a holistic unit.
- Coupling the models by an innovate mapping approach.
- VOF-to-DPM coupled with Adaptive Mesh Refinement technique employed.
- The effect of flow field inside the nozzle on the liquid sheet characteristics.

GRAPHICAL ABSTRACT

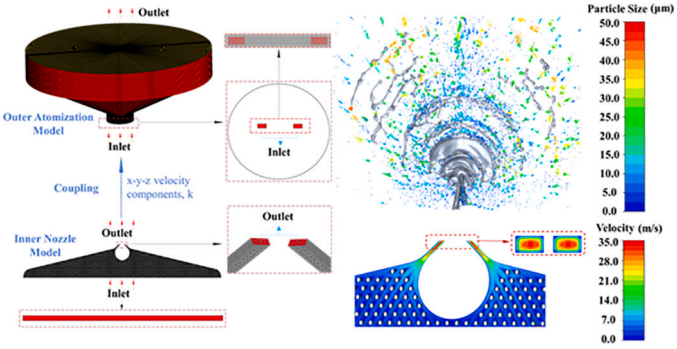

ARTICLE INFO

Keywords:
Impinging jet atomization
Computational fluid dynamics
VOF-DPM
Mapping approach
Jet dynamics

ABSTRACT

Impinging jet atomization is a new approach in inhalation therapy for drug delivery. Numerical simulation is a powerful tool for pursuing better understandings of the impinging jet dynamics. However, it is an extremely challenging task to simulate atomization of soft mist inhalers due to their complex nozzle geometry and spatial-temporal evolution of jets and droplets whose sizes span multiple orders of magnitude. In this work, the atomization process was simulated by a Computational Fluid Dynamics (CFD) model that couples the Volume of Fluid method (VOF), Discrete Phase Model (DPM), and Adaptive Mesh Refinement (AMR). A mapping approach was used to efficiently couple the liquid flow inside the small-scale nozzle with the large-scale multiphase jet flow outside the nozzle. The influence of flow field inside the nozzle on the atomization characteristics was explored. The numerical and experimental jet dynamics are consistent with regard to the plume geometry and particle size distribution. It was revealed that with the increase of the impingement angle and nozzle inlet pressure, the fluctuation of liquid sheet becomes more violent, which directly affects the breakup pattern and leads to much finer droplets. This method can be used to optimize the inhalers for better atomization performance.

* Corresponding author at: School of Energy and Environment, Southeast University, Nanjing 210096, China.
** Corresponding author.
E-mail addresses: jie.xiao@suda.edu.cn (J. Xiao), z.tong@seu.edu.cn (Z. Tong).

https://doi.org/10.1016/j.powtec.2022.117622
Received 8 April 2022; Received in revised form 24 May 2022; Accepted 10 June 2022
Available online 15 June 2022

Nomenclature

a	length of the rectangular nozzle (m)
b	width of the rectangular nozzle (m)
C_D	drag coefficient
d	hydraulic diameter of the jet (m)
d_p	particle diameter (m)
$\vec{F}$	force of surface tension between two phases
k	turbulent kinetic energy (kg m^2 s^{-2})
m_p	particle mass (kg)
n	index for current time step
$\vec{n}$	surface normal vector
$\vec{n}$	surface normal vector
$\hat{n}$	unit vector normal to the face
p	pressure (kg m^{-1} s^{-2})
Re	relative Reynolds number
t	time (s)
U_f^n	volume flux through the face at time step n (m^3 s^{-1})
$\vec{u_j}$	velocity of the liquid jet
$\vec{u_p}$	particle velocity (m/s)
V	cell volume (m^3)
V_X	velocity component in the X direction
$\vec{v_j}$	velocity of jets (m/s)
$\vec{v_l}$	velocity of liquid phase (m/s)
We	Weber number

Greek symbols

α	phase volume fraction
α_g	phase volume fraction of gas phase
α_l	phase volume fraction of liquid phase
$\alpha_{l,f}^n$	face value of the liquid phase volume fraction at time step n
κ	free surface curvature
μ	dynamic viscosity (kg m^{-1} s^{-1})
ρ	density (kg m^{-3})
ρ_l	density of liquid (kg m^{-3})
σ	surface tension coefficient (kg s^{-2})
τ_r	relaxation time (s)
φ	half of the impingement angle (°)

Superscripts

n	index for current time step

Subscripts

g	gas phase
j	liquid jet
l	liquid phase
p	particle
w	water

1. Introduction

Inhalation therapy is a crucial administration route which allows delivering the drug to the respiratory tract and lungs through inhalation. The drug can be made into forms of aerogel, dry powder or atomized droplets, resulting in effective cure for obstructive lung diseases [1]. The delivery efficiency of inhaled drugs greatly depends upon the type of drug delivery device adopted, which directly determines the delivered dose and deposition percentage in the lung [2]. At present, the most widely-used inhaler device is Respimat® Soft Mist™ Inhaler (SMI), an innovative type of liquid inhaler [3].

In Respimat®SMI, the drug is split into two jets that impact at a fixed angle by the nozzle through the mechanical energy obtained by spring compression [4]. The jet collision produces a slow-moving soft mist that allows for high drug delivery efficiency. The particles must be in the range of 0.5–5 μm in order to be directly delivered to the target bronchioles and alveoli [5]. Given the high percentage (65%–80%) of fine particles (1–5 μm) and the slow-moving soft mist (0.8 m/s) produced by Respimat®SMI [6], the drug can be administered to the lungs in a slow and controlled way, reducing inertial deposition in the oropharynx and improving lung deposition rates, which can reach 40% on average for adults [7]. The release time of Respimat® SMI spray is long (1.2–1.5 s), which facilitates hand-breath coordination [8]. Respimat®SMI advances the development in route of administration significantly.

The Respimat®SMI has a micron chip called Uniblock with filtered structure, which is the core element for atomization, and its nozzle structure produces spray based on the principle of atomization by impinging jets [8]. Lots of experimental and numerical studies have been made by scholars in the field of double-jet impingement atomization. Taylor derived the thickness distribution and the shape of the liquid rim by analyzing the small disturbances on liquid sheet [9]. Heidmann analyzed the factors influencing the disintegration of liquid sheet and related the disintegration to jet velocity [10], while Tanasawa considered the disintegration mechanisms to be the function of Reynolds number of liquid jets [11]. Dombrowski et al. experimentally investigated atomization by impingement of laminar jets and turbulent jets and concluded that the influencing factors of liquid sheet breakup were jet velocity profiles and impingement angle. His study showed that liquid sheet fragmentation resulted from hydrodynamic and aerodynamic waves, with the latter dominating the fragmentation at higher Weber numbers and larger impingement angles [12]. Huang also investigated the disintegration mechanisms of liquid sheet and found that there were two distinctive breakup regimes of liquid sheet at different Weber number. The Kelvin-Helmholtz instability of the liquid sheet was analyzed to derive the particle size distribution when Weber numbers were above 2000 [13]. However, Huang's theoretical analysis only resulted in wave speed expression. Based on the breakup regime proposed by Huang [13], Ibrahim et al. developed analytical models to predict the shape and thickness of the sheet in the breakup regime at low Weber number and the droplet size distribution at high Weber number [14]. Li et al. obtained the fragmentation length and the size of the liquid sheet from Ibrahim's predicted model of liquid sheet shape [15]. Santoro et al. explored the formation of impact wave and its influence on atomization process through experiments, finding that the characteristic wavelength of the impact wave was one jet diameter and that the distance between waves increased with distance from the impingement point [16]. Bailardi et al. studied the spray patterns of Newtonian fluids injected by identical impinging nozzles at high Weber numbers and obtained seven main modes of fragmentation at different Weber and Reynolds numbers [45].

The studies above were all based on results obtained from experimental and theoretical analyses. With the fast development of the computational power, the numerical simulation of jet impingement atomization plays a more important role in investigating the underlying physics of impinging jet dynamics. The numerical studies of atomization process involve multi-scale simulations for the scales of droplets and liquid bulk vary by several orders of magnitude. Most studies focused on the idea of coupling of Eulerian method and Lagrangian method to solve the scale difference. The dynamically evolving phase interface is calculated by Eulerian formulations, while small droplets in the flow field are readily identified and tracked using the Lagrangian Particle Tracking (LPT) method. According to the different Eulerian method, the multi-scale simulation approaches of atomization process can be classified as LS (Level Set)-based approach, VOF (Volume of Fluid)-based

approach and CLSVOF (Coupled Level Set and Volume of Fluid)-based approach [18].

In the LS-based approach, liquid lumps are tracked using the LS method, while small droplets are tracked using the LPT method. For example, Luo et al. applied LS method combined with a curvature-based correction to investigate the atomization process [19]. Himeno et al. used 'CIP-LSM' (CIP based Level Set & MARS) simulations to investigate the phenomenon of colliding atomization of two coaxial jets. This method allowed for more accurate calculation of volume fractions and thus a clearer capture of the interface between two phases [20]. Kim et al. simulated the primary breakup of liquid jet by a Refined Level Set Grid (RLSG) method in combination with a Lagrangian model [21]. Herrmann et al. have also used the same approach to explore atomization process in crossflow [22].

VOF-based approach describes the motion of large liquid masses using VOF method, while tracking the motion of small droplets by DPM method. Gorokhovski et al. used the VOF method to explore the primary breakup process of a jet flow through a single nozzle at the millimeter scale [23]. Chen et al. used VOF method combined with AMR to analyze the atomization characteristics of impinging jets through circular nozzles of 400 μm and 600 μm in diameter at low and high speed, respectively. High-fidelity simulations of liquid sheet breakup patterns were obtained [24]. Based on the two-phase VOF solver, Tomar et al. proposed a Eulerian-Lagrangian two-way coupling method, and effectively predicted the collision between two particles by spatial hashing algorithm [25]. *Ma* et al. investigated the patterns and breakup features of liquid sheets using high-fidelity simulations. A three-dimensional VOF method based on AMR with octree grid was applied as well [26]. The coupled VOF-DPM model introduced in Fluent 19.0 has also applied this method, so the two-phase multiscale simulations of atomization can be realized.

CLSVOF-based method uses Level Set to identify the gas-liquid interface accurately while reducing mass loss by the VOF method. Menard et al. solve discontinuities at sharp interfaces using combined CLSVOF and the Ghost Fluid Method (GFM) [27]. Zheng et al. conducted numerical simulations of impinging jet atomization using millimeter-scale nozzles at impingement angles of 50° and 80° by the CLSVOF method and found that the impingement angle affects the amplitude of fluctuations of the liquid sheet, thus affecting ligaments fragmentation and particle size distribution [28]. Li et al. used CLSVOF coupled with Lagrangian algorithm to track the interface between liquid and gas, as well as the trajectories of droplets [29].

At present, many numerical simulations of double-jet impingement atomization based on Euler-Lagrange integration methods have been carried out, but the fluid flow inside the nozzle has been neglected, while the three-dimensional atomization simulation of impinging jet through micron-sized rectangular nozzles has not been studied. Based on the previous work, this study further combines the new VOF-to-DPM model with the mapping approach to develop a numerical simulation method suitable for analyzing dynamics of impinging jets through micron-scale nozzles or nozzles with complex structures. This method can effectively couple models of the small-scale nozzles and the large-scale atomization space. The effectiveness of the method is demonstrated through the case study of the Respimat®SMI. The influences of jet velocity and impinging angle on flow patterns, particle size distribution and velocity distribution near the impingement point were investigated. Based on the analyses, the regulation mechanism of atomization performance was further revealed. This simulation method can be widely used in future to optimize the structure of nozzle to provide efficient and optimal atomization.

2. Modeling and analysis method

2.1. System geometry and operating conditions

The nozzle configuration of Uniblock in Respimat®SMI was adopted as the case study to explore the dynamics of impinging jets atomization. In this work, the computational nozzle system was divided into two models: inner nozzle model and outer atomization model.

For the inner nozzle model, the geometric sizes were adjusted to optimize the structure design. As shown in Fig. 1 (a), the original Uniblock contains primary structures in the lower part and secondary structures in the upper part of the nozzle. These structures comprise channels located between projections in the shape of circular or rectangular which were arranged side by side in rows in order to filter the drug solution. As the primary structure has insignificant effects on the atomization effect based on the initial investigation, numerical models only adopted the upper part of Uniblock nozzle containing secondary structures. The structure and detailed sizes of nozzle model were shown in Fig. 1 (b). The size of nozzle is $100 \times 50\ \mu m^2$. The impingement angle (2φ) of 60° and 90° were chosen. Fig. 2 indicates the grid system of inner nozzle model. Given the extreme thinness of the inner nozzle model, the meshing technique of stretching the 2D surface mesh to 3D unstructured mesh was used. Finer mesh was used in the nozzle region with grid length of 5 μm (see Fig. 2 (b)). The overall cell number is 1335240, with the maximum cell volume of $4.6 \times 10^{-15}\ m^3$ and the minimum cell volume of $2.43 \times 10^{-17}\ m^3$. The pressure of inlet was 5 bar, 7 bar and 14 bar, which was common value of pressure applied to nebulizer devices [31]. The outlet was set as pressure outlet with gauge pressure of zero.

Fig. 2 (a) indicates the computational system of full-scale three-dimensional outer atomization model. Structured grid was used and the number of hexahedral cells is 3,077,494. The maximum size of the cell is $2.82 \times 10^{-10}\ m^3$, while the minimum size is $2.53 \times 10^{-16}\ m^3$ upstream of the impingement point and $8.14 \times 10^{-13}\ m^3$ downstream of the impingement point, and the average quality of the mesh is 0.936. To capture the detailed dynamics of jets, finer grids were arranged around the nozzle. The number of grid cells at the long and wide edges of the nozzle is 10 and 5, respectively.

In the atomization simulation. The Adaptive Mesh Refinement technique (AMR) was used to refine/coarsen specific mesh. Regions near the interface of the liquid and gas are refined with grids in small length scale to capture topology changes. The AMR in this study used gradient-based criteria of volume fraction, because VOF has high gradient on the interface and gradient-based algorithm can guarantee adequate refined grids and prevent excessive dissipation of kinetic energy [24]. The minimum cell size of refine level was limited to $10^{-18}\ m^3$. Table 1 indicates the simulated material properties. The solver settings for outer atomization model in ANSYS Fluent are shown in Table 2. The VOF-to-DPM model was adopted to automatically convert liquid mass detached from the liquid core to particles. The secondary breakup of the atomization was solved by the Taylor Analogy Breakup (TAB) model. In this study, the computational cost of atomization simulations is expensive. For each of the case, the simulation was performed on 85 processors and the calculation time took about 672 h (around 1 month).

To establish flow field throughout the inner and outer zone of nozzle, a mapping approach was adopted. As shown in Fig. 2, the inner nozzle model was initialized with fixed pressure at the inlet and gauge pressure of zero at the outlet. The flow field data involving velocity and turbulence intensity obtained from the outlet of inner nozzle model were mapped to the inlet of outer atomization model. These data were served as the input conditions for the outer atomization model. This procedure enables the transfer of the flow field information through the nozzle system, effectively solving the multi-scale differences between the nozzle and the external space, meanwhile significantly saving computational costs. It is an innovative numerical simulation method suitable for analyzing impinging jets through micron-scale nozzles or nozzles with complex structure.

2.2. Governing equations

The VOF-to-DPM model was used to simulate the transition process of liquid stream from continuous phase to discrete phase. The model

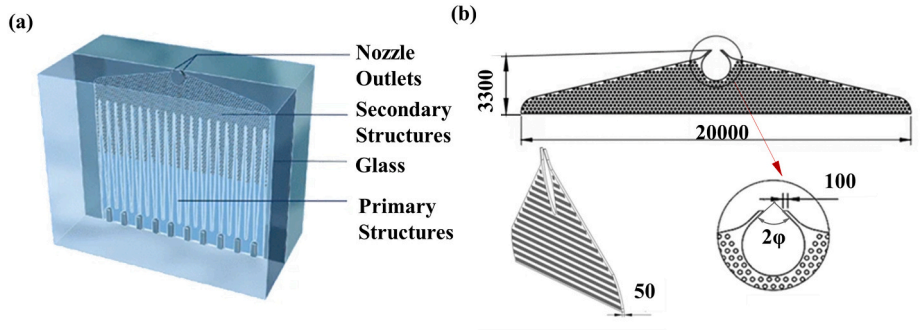

Fig. 1. Structure diagram of nozzle: (a) original Uniblock structure [30], (b) numerical inner nozzle model. (Dimension: μm).

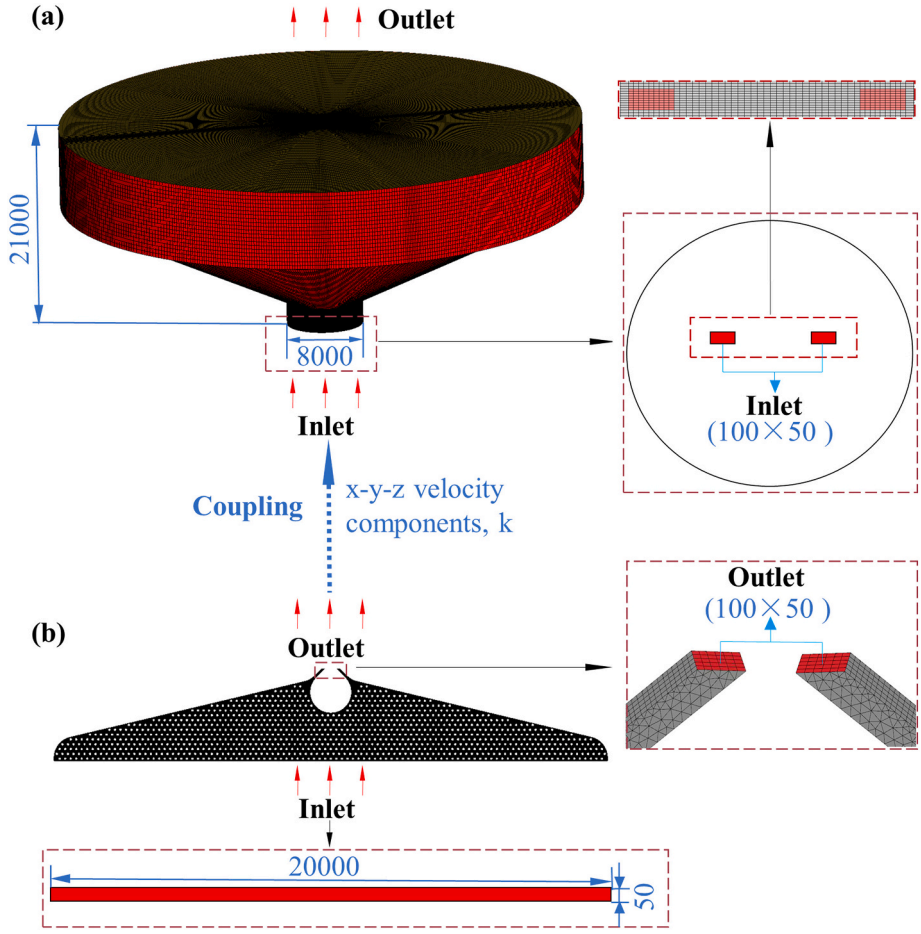

Fig. 2. Schematic diagram of the computational nozzle system and coupling scheme of the mapping approach: (a) outer atomization model, (b): inner nozzle model. (Dimension: μm).

Table 1
Material properties.

Material properties	Primary phase	Secondary phase
Fluid material	Air	Water
$\rho/(kg \bullet m^{-3})$	1.225	1000
$\mu/(kg \bullet m^{-1} \bullet s^{-1})$	1.7894×10^{-5}	0.001
$\sigma/(N \bullet m^{-1})$	–	0.072

uses the VOF algorithm to trace the gas-liquid interface, thus capturing initial atomization of the liquid sheet. For droplets leaving the liquid core, if the transition standards are met, the DPM method is used to track and obtain particles information including their trajectory and particle size distribution etc. Therefore, this model can be used for the numerical simulation of the double-jet atomization phenomenon.

The VOF method is an interface-tracking method based on the Euler equation by keeping track of the volume fraction of air and liquid throughout the domain. In a grid cell, the continuity equation is:

$$\frac{1}{\rho_l}\left[\frac{\partial}{\partial t}(\alpha_l\rho_l) + \nabla\cdot(\alpha_l\rho_l\overrightarrow{v_l})\right] = 0 \quad (1)$$

where ρ_l, $\overrightarrow{v_l}$ are the density (kg/m^3) and velocity (m/s) of the liquid phase respectively. The constraint used to compute the volume fraction of fluids is as follows:

$$\alpha_l + \alpha_g = 1 \quad (2)$$

Table 2
Summary of solver settings for outer atomization model.

Time	Transient, 1st Order Implicit
Multi-phase model	VOF-to-DPM
VOF model	Explicit; Geo-Reconstruct
Secondary breakup	Taylor Analogy Breakup (TAB)
Viscous model	SST k-ω, Stress-Blended Eddy Simulation (SBES) Model
Pressure-Velocity coupling	PISO
Momentum discretization method	2nd Order Upwind
Pressure discretization method	PRESTO!
Volume fraction discretization method	Geo-Reconstruct
Shear condition	No slip
Time step/s	1×10^{-8}
Surface tension	Continuum Surface Force (CSF)

The time-dependent explicit VOF model is used to solve the volume fraction equation of liquid by discretizing the volume fraction in the following way:

$$\frac{\alpha_l^{n+1}\rho_l^{n+1}-\alpha_l^n\rho_l^n}{\Delta t}V+\sum_f \rho_l U_f^n \alpha_{l,f}^n = 0 \tag{3}$$

where n is the number of steps, $\alpha_{l,f}$ is the face value of the liquid phase volume fraction and V is the cell volume (m^3).

The momentum conservation equation in an inertial system is:

$$\frac{\partial}{\partial t}(\rho\vec{v})+\nabla\cdot(\rho\vec{v}\vec{v}) = -\nabla p+\nabla\cdot[\mu(\nabla\vec{v}+\nabla\vec{v}^T)]+\rho\vec{g}+\vec{F} \tag{4}$$

where F is the force of surface tension between two phases (N), and the continuum surface force (CSF) model proposed by Brackbill et al. is used which consider surface tension as a continuous effect and is suitable for the fluid flow affected by interfacial surface tension [32]. The expressions are as follows:

$$F=\sigma_{ij}\frac{\rho\kappa_i\nabla\alpha_i}{\frac{1}{2}(\rho_i+\rho_j)} \tag{5}$$

where σ is the surface tension coefficient (N/m), κ represents the free surface curvature, $\vec{n}$ is the surface normal vector and $\hat{n}$ is the unit vector normal to the interface:

$$\vec{n}=\nabla\alpha_l \tag{6}$$

$$\kappa=\nabla\cdot\hat{n} \tag{7}$$

$$\hat{n}=\frac{\vec{n}}{|n|} \tag{8}$$

Both density and viscosity of two phases follow the law of mixtures and the equations are as follows:

$$\rho=a\rho_l+(1-a)\cdot\rho_g \tag{9}$$

$$\mu=\alpha\mu_l+(1-\alpha)\cdot\mu_g \tag{10}$$

For discrete phase particles, the governing equations are grounded in Lagrangian framework. The particle motion is determined by force balance differential equations based on the Newton' s second law, which can be written as:

$$m_p\frac{d\vec{u_p}}{dt}=m_p\frac{\vec{v_l}-\vec{u_p}}{\tau_r}+m_p\frac{\vec{g}(\rho_p-\rho)}{\rho_p}+\vec{F} \tag{11}$$

where m_p is the particle mass (kg), $\vec{v_l}$ is the liquid phase velocity (m/s), $\vec{u_p}$ is the particle velocity (m/s), ρ is the fluid density (kg/m3), $\rho_p$is the density of particle (kg/m3), $m_p\frac{\vec{u}-\vec{u_p}}{\tau_r}$ is the drag force (N) and τ_r is the relaxation time (s) calculated by:

$$\tau_r=\frac{\rho_p d_p^2}{18\mu}\frac{24}{C_d R_e} \tag{12}$$

where μ is the liquid viscosity (Pa•s), d_p is the particle diameter (m), Re is the relative Reynolds number, which is defined as:

$$Re=\frac{\rho d_p\left|\vec{u}_p-\vec{v_l}\right|}{\mu} \tag{13}$$

C_D represents the drag coefficient between the particle and the air. Given the particles are smooth spheres, the spherical drag model is used:

$$C_D=a_1+\frac{a_2}{R_e}+\frac{a_3}{R_e^2} \tag{14}$$

where a_1, a_2, a_3 use different constants for different Re numbers according to Moris and Alexander [33].

The VOF-to-DPM model transition algorithm seeks to detect lumps apart from the liquid core which are solved using VOF method. The lumps must satisfy both size and shape criteria to get elected for transition to particles. The size-based criteria were set as 0–50 μm based on the experimental results of particle size distribution. Meanwhile, the shape of liquid lump is characterized by asphericity and the maximum asphericity is set as 0.5 empirically. If volume-equivalent sphere diameter of liquid lumps is within the range of 0–50 μm and the asphericity is below 0.5, the liquid lump will be converted to Lagrangian particle parcels. Characteristics of the particles in the parcel can be analyzed, thereby obtaining the particle size distribution.

2.3. Analysis method

Fig. 3 indicates the schematic diagram of double-jet impingement atomization. Two jets at high velocity $\vec{u_j}$ are ejected from a rectangular nozzle and collide at angles of 2φ. The jet dynamics was characterized by the dimensionless parameter Weber number and Reynolds number, defined as [34]:

$$We=\frac{\rho\vec{u_j}^2 d}{\sigma} \tag{15}$$

$$Re=\frac{\rho\vec{u_j}d}{\mu} \tag{16}$$

where ρ is the density of the liquid (kg/m^3), d the hydraulic diameter of the jet (m), $\vec{u_j}$ the mean jet velocity (m/s), σ the surface tension of the water (N/m) and μ the dynamic viscosity of the water (pa•s).

When two identical jets collide, the momentum of each jet in the X direction decreases rapidly under the influence of the great impact force generated. The velocity components in the direction of X-axis $\vec{u_x}$ and Y-axis $\vec{u_y}$ at the central axis of two jets were chosen to investigate the velocity change near the impingement point, thus inferring the magnitude of the impact force. $|L|$ represents the distance from a certain point on the central axis of liquid jet to the impingement point, while the additive inverse of the distance was adopted for jet on the opposite side of the spray axis (see Fig. 3 (c)). After colliding of two identical jets, an expanding liquid sheet is formed in a direction perpendicular to the plane containing axes of the two jets [35]. The impact waves originated from the impingement point cause violent flapping of the liquid sheet, leading to breakup of liquid sheet into ligaments and droplets subsequently. The breakup length is referred to as the distance from the impingement point to where the liquid sheet breaks up along the spray axis (see Fig. 3 (a)) [36]. A plane is created at 1.5 mm from the nozzle to obtain the droplet particle size distribution (see Fig. 3 (b)).

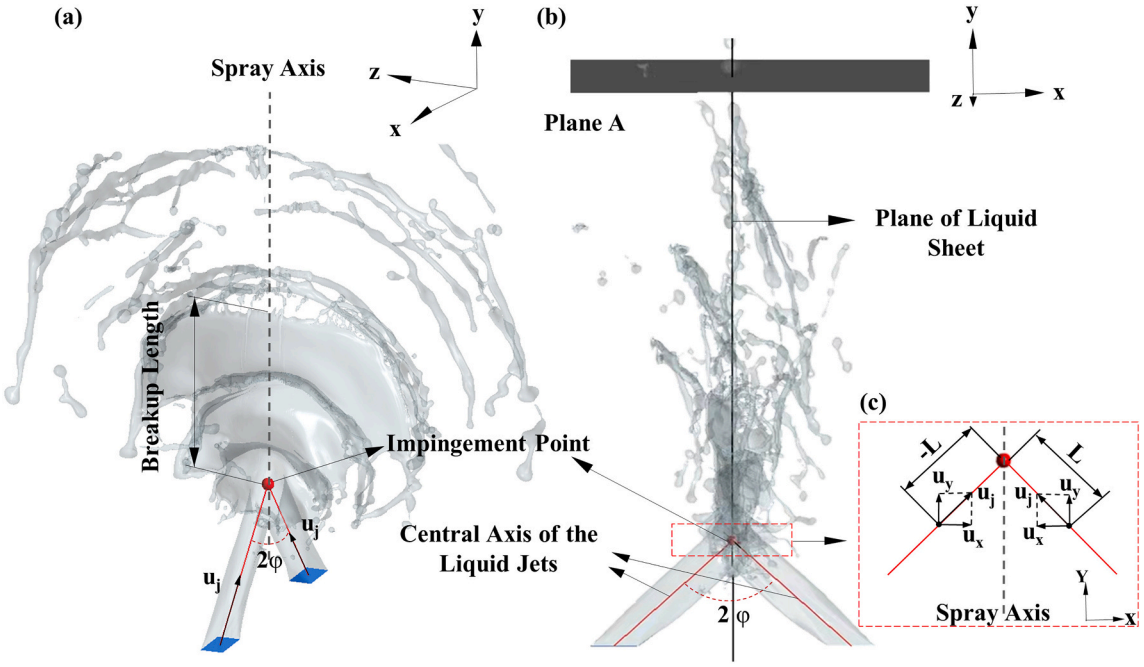

Fig. 3. Schematic diagram of double-jet impingement atomization: (a) overview of jets and liquid sheet, (b) sideview of jets and liquid sheet, and (c) data collection scheme for velocity profile of liquid jets.

3. Results and analysis

3.1. Model validation

The particle size distribution and plume angle from simulation were compared with the experimental results with regard to both trends and magnitudes.

In simulation, a plane was created at 1.5 mm from the nozzle to record DPM particles that passed through the plane during flow time from 0.06 ms to 0.07 ms. The cumulative distribution of particle size was calculated and compared with experimental data tested by the laser diffraction particle analyzer (Sympatec, Pennington, New Jersey). The results show that the predicted particle size is overall smaller than the experimental values at the same cumulative percentage as shown in Fig. 4, while the average relative deviation is less than 15% (see Table 3). In addition, the angle of simulated plume is in good agreement with experimental result. The validation proves that the model can characterize the process of impinging jet atomization well. The reasons of the existence of small deviation in particle size distribution can be attributed to several factors. First, the atomization time in simulation is shorter compared to the experimental time because of the limit in computational resources. Second, Mansour et al. has found that the particle diameter decreases initially due to secondary breakup, and increases subsequently along the spray axis because of droplet coalescence [37]. The coalescence process was not taken into account in our study, which led to underestimation of drop size. Third, the grid resolution is not high enough to capture the exact motion of liquid-gas interface of the atomization process.

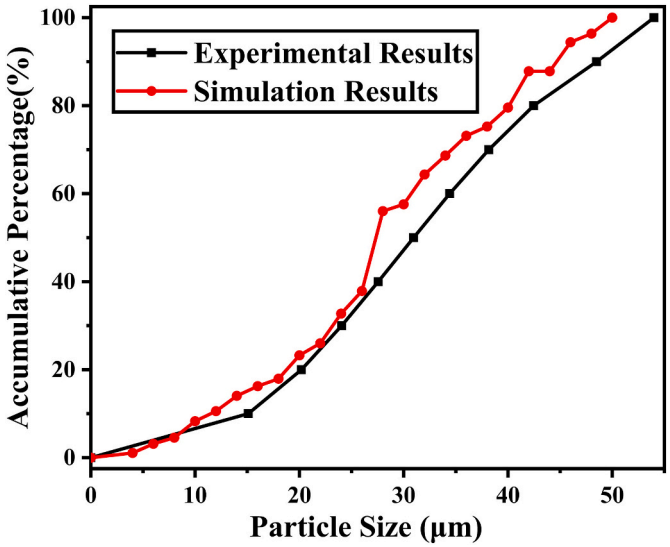

Fig. 4. Comparison of accumulative percentage distribution between experimental results and simulation results.

3.2. Atomization process

Fig. 5 indicates the temporal evolution of the liquid sheet generated by impinging jets through complete nozzle system. It shows the whole atomization process including fluid flow inside the nozzle, the formation of impinging jets and liquid sheet, the disintegration of liquid sheet into ligaments and droplets subsequently. The flow field inside the nozzle was shown in Fig. 5 (b). The velocity of the fluid increases near the nozzle outlets and the velocity distribution at the nozzle outlet is uneven. The velocity value reaches the highest in the center of the nozzle exit and decreases to zero near the wall. The velocity distribution of the outlet of inner nozzle model is mapped to the inlet of outer atomization model to couple inner and outer zone of the nozzle. The effectiveness of mapping approach is introduced later in details.

The jet dynamics in the outer atomization space was shown in Fig. 5 (a). The water-gas interface is visualized by the isosurface of liquid phase volume fraction at 0.5. A fan-shaped liquid sheet is formed at 0.04 ms. The edge of the liquid sheet breaks up under the surface tension between gas and liquid, forming ligaments in the downstream region and a small number of fine particles near the liquid rim. Slight fluctuation originated from the impingement point appears on the surface of the liquid sheet. Impact waves appear at 0.05 ms, leading to violent flapping of the liquid sheet which disintegrates into liquid core region

Table 3
Comparison of cumulative percentage of particle size diameter between the numerical and experimental results.

Cumulate percentage		10%	20%	30%	40%	50%	60%	70%	80%	90%	100%
Particle size diameter (μm)	Experimental results	15.10	20.19	24.05	27.55	30.95	34.41	38.16	42.46	48.49	54.00
	Simulation results	11.50	18.78	23.19	26.23	27.34	30.59	34.60	40.02	45.32	50.00
Relative error (%)		23.84	6.98	3.58	4.79	11.66	11.10	9.33	5.77	6.54	7.41

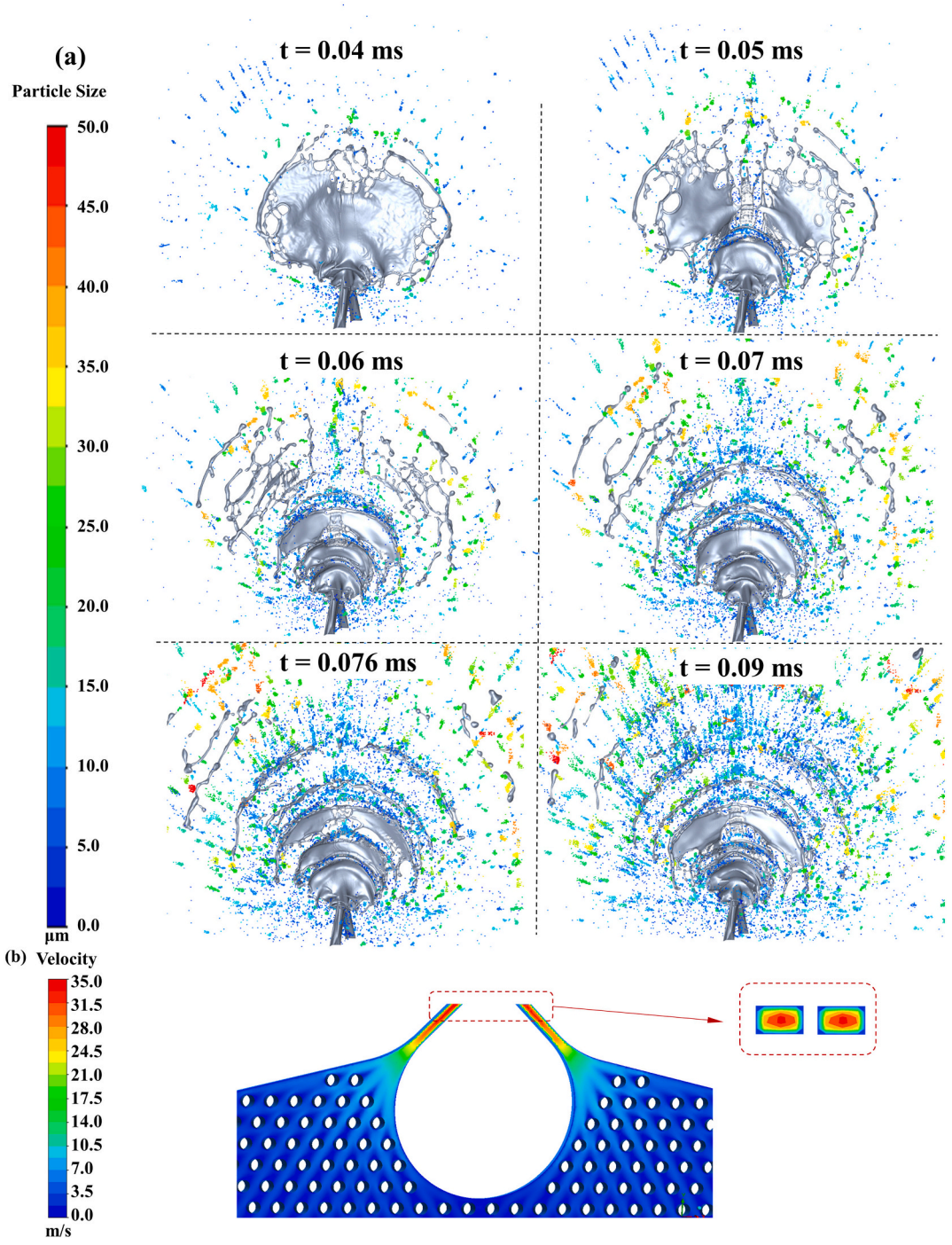

Fig. 5. Temporal evolution of flow fields: (a) formation and fragmentation of liquid sheet, and particle size distribution at different instants, (b) velocity distribution of the nozzle outlet and central plane of nozzle vertical to nozzle outlet. (a × b = 100 × 50 μm^2, $\bar{u}_j$= 27.6 m/s, 2φ = 90°, *We* = 705, *Re* = 1844).

and ligament region where many holes are formed. Larger particles appear near the rim of liquid sheet due to the breakup of ligaments. From 0.05 ms to 0.06 ms, impact waves grow and propagate downstream. The intense destabilization of liquid sheet causes the increasing number of ligaments and subsequently lead to increasing number of particles, especially large ones occurred near the ligaments.

U-shaped ligaments are formed at 0.07 ms. The length of the liquid core region seems to remain unchanged over the period from 0.07 ms to 0.09 ms, while the distance between ligaments increases radially outward from the impinging point. Meanwhile, there is an obvious increase in the amount and spatial coverage of the particles in the period of 0.05 ms to 0.09 ms.

Fig. 6 indicates the spatial evolution of the liquid sheet and ligaments for the nozzle model at 90° impingement angle with inlet pressure of 7 bar. It's indicated that the liquid sheet is divided into liquid core region and ligament region. The liquid core region is fan-shaped, representing the impingement of jets and flapping of liquid sheet. The disturbances induced by the impact waves propagate radially outward along the liquid core, causing violent fluctuations and disintegration. Thick liquid bands are formed at the fracture due to surface tension and aerodynamic forces. Many thin ligaments are formed longitudinally and horizontally between the edge of the liquid core and the thick liquid bands. These cross-linking ligaments compose liquid bridges [38] (see Fig. 6 (b)). The ligament region is distributed with irregularly shaped holes, which is caused by the wide variation of sheet thickness and the fluctuating along the radial direction, as shown in Fig. 6 (a). The holes get elongated with jagged edges due to the movement of the ligament region. The ligaments are formed owing to the rupture of liquid bridges as the holes approach the edge of the liquid sheets. The ligaments are U-shaped and the distance between the ligaments increases radially. The ligaments subsequently break up to form shorter ligaments, which then break off into droplets (see Fig. 6 (c)).

To demonstrate the efficacy of the introduced mapping approach, the flow field data of center line located on the outlet surface of inner nozzle model (Model A) were compared with corresponding location of outer atomization model (Model B). The flow field information involves turbulent kinetic energy (k), velocity magnitude, velocity component in the X direction (V_x), Y direction (V_y) and Z direction (V_z). As shown in Fig. 7, flow field information can be perfectly mapped between individual models by mapping approach, realizing the numerical coupling of the whole nozzle system as a holistic unit.

3.3. Effect of pressure on atomization process

The effect of inlet pressure on atomization process was investigated in this set of simulations. The nozzle model with impingement angle of 90° was used as the base model. The parameters of nozzle model under different inlet pressure were shown in Table 4. Only the pressure at the inlet of the nozzle model was changed, thereby changing the mean jet velocity at the nozzle exit, and then the influence of jet velocities on the spray field was analyzed.

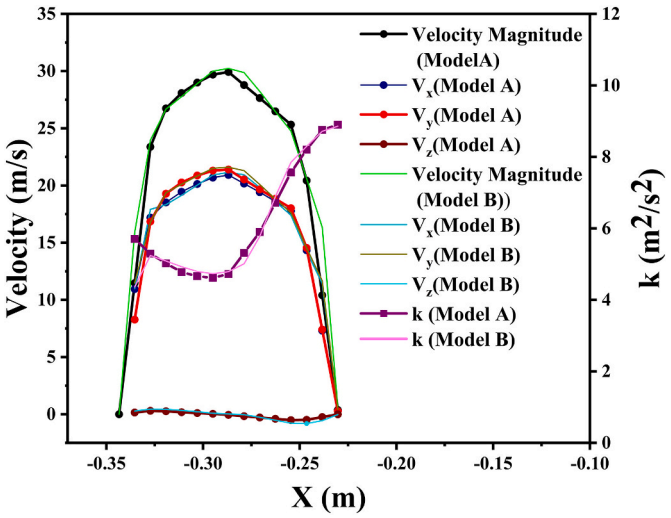

Fig. 7. Comparison of velocity profiles and turbulent kinetic energy profiles on the center line of one nozzle between inner nozzle model A and outer atomization model B. (a × b = 100 × 50 μm^2, $\bar{u}_j$= 22.7 m/s, 2φ = 90°, *We* = 477, *Re* = 1516).

3.3.1. Liquid sheet pattern analysis

Fig. 8 (a), (b) and (c) show the velocity contours of inner zone of nozzle and liquid sheet at 0.07 ms for the Case 1–1, 1–2 and 1–3. It's indicated that the pressure of the nozzle inlet affects flow condition at the nozzle exit. The velocity of the nozzle exit increases significantly as pressure increases, with higher velocity gradient at the nozzle exit, leading to more unstable disturbances embedded in the jet [39]. Growth of surface instability caused by disturbances in jet affects the subsequent disintegration of liquid sheet. Meanwhile, impact waves generated by impingement of jet at higher Weber number grow faster with larger

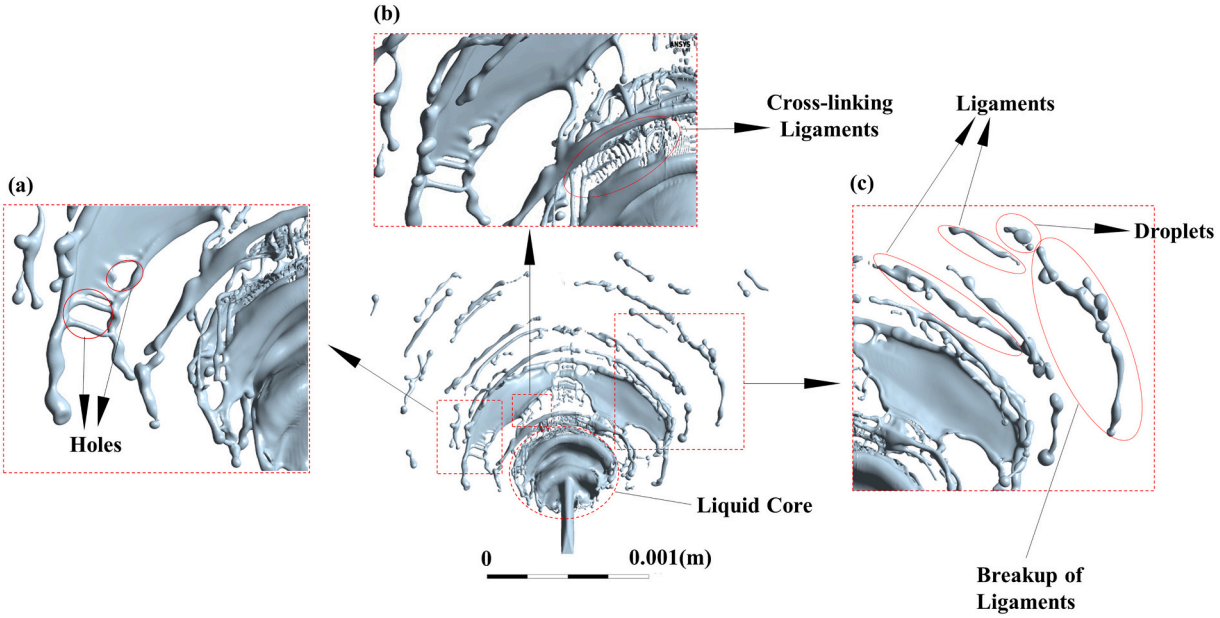

Fig. 6. Spatial evolution of the liquid sheet and ligaments at 0.09 ms. (a × b = 100 × 50 μm^2, $\bar{u}_j$= 27.6 m/s, 2φ = 90°, *We* = 705, *Re* = 1844).

Table 4
Parameters of nozzle model under different pressure.

Case	Impingement angle (°)	Nozzle size (μm^2)	Time (ms)	Inlet pressure (bar)	Mean jet velocity (m/s)	Weber number	Reynolds number
1–1	90	100 × 50	0.0693	5	22.7	477	1516
1–2	90	100 × 50	0.07	7	27.6	705	1844
1–3	90	100 × 50	0.0698	10	34.1	1077	2278

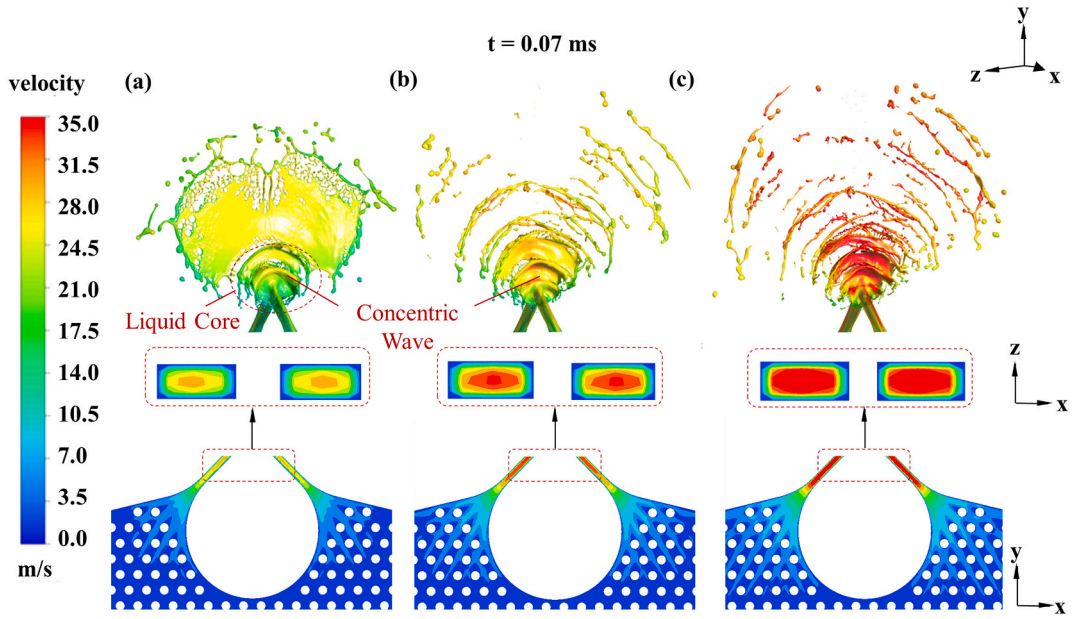

Fig. 8. Comparison of velocity distribution of the nozzle exit, central plane of nozzle vertical to nozzle exit and liquid sheet between different inlet pressure: (a) $p = 5$ bar, $\overline{u}_j = 22.7$ m/s, $We = 477$, $Re = 1516$ (b) $p = 7$ bar, $\overline{u}_j = 27.6$ m/s, $We = 705$, $Re = 1844$ (c) $p = 10$ bar, $\overline{u}_j = 34.1$ m/s, $We = 1077$, $Re = 2278$. (a × b = 100 × 50 μm^2, $2\varphi = 90°$).

amplitude. The Kelvin-Helmholtz waves in liquid sheet also become stronger due to the increase of sheet velocity relative to the ambient air, which directly affects the breakup pattern of the liquid sheet [40]. Therefore, the velocity profiles of jet at the nozzle outlet affected by the flow conditions inside the nozzle, have a crucial influence on the atomization characteristics.

The liquid rim and sheet show different structures at different Weber number and Reynolds number. At lower Weber number and Reynolds number, the unstable rim pattern is shown in Fig. 8 (a) [41]. Concentric impact waves generated cause high-amplitude fluctuation at the liquid core region, but are damped out rapidly. In addition, the downstream region of the liquid is disturbed by the interaction force of liquid and gas, giving rise to the formation of small holes. The unstable liquid rim with enlarging holes causes disintegration of liquid sheet to ligaments. Lower ligaments are influenced by perturbative self-increasing effect due to surface tension, also known as the Rayleigh-Plateau effect [42], which causes the ligaments breakage into droplets. As the Weber number and Reynolds number increase, the mean jet velocity increases accordingly, resulting in more intense fluctuation of the liquid sheet (see Fig. 8 (b) and (c)). This pattern is called the impact wave pattern [40]. The liquid rim is totally fragmented into U-shaped ligaments due to the impact wave. As the velocity of sheet is higher than that of the gas, the gas-liquid interaction generates K—H waves that dominate the breakup of the sheet. K—H instability is amplified and propagates fast along the liquid sheet. Therefore. the liquid sheet becomes more unstable and fluctuates more vigorously until it reaches its critical amplitude and breaks up into ligaments. This gives rise to the increase in the amount and spatial coverage of ligaments.

3.3.2. Mesh adaption and interfacial dynamics

The Interfacial dynamics and numerical grids at x-y cut section view in mid-plane of the outer atomization model is shown in Fig. 9. Fine grids in the liquid-gas interface region generated by the AMR technique allow accurate characterization of the interfacial dynamics of liquid sheet. The grids are refined locally with a refinement level of 4, which means the initial cell number will be increased by $(2^4)^3 = 4096$ times if the same resolution is required with a uniform mesh. Therefore, AMR can greatly reduce the computational efforts. Sharp interface at the fracture of thin sheet is well resolved with a minimum cell length of 0.8 μm for three cases.

When the jet velocity rises, the surface fluctuation on the liquid sheet becomes more intense, with an increase in wave number and a decrease in wave length at higher Weber number and higher Reynolds number. The distance between upper and lower surfaces of liquid sheet decreases outward from the impingement point due to the motion of the liquid rim, and the liquid sheet tends to reach its thinnest state and fracture near the crest or trough of the wave. As shown in Fig. 9 (a), the impact waves are initially formed near impingement point and then damped out quickly, resulting in insignificant fluctuations in the downstream region and longer ligaments. When the jet velocity rises, the amplitude of impact waves spontaneously intensifies [43], which gives rise to more thorough fragmentation at higher Weber number (see Fig. 9 (b) and (c)).

3.3.3. Particle size distribution analysis

Particle size is an essential parameter to characterize the atomization effect. Planes are created at 1.5 mm from the nozzle (see Fig. 3 (b)) to record DPM particles which passed through the plane during flow time from 0.05 ms to 0.06 ms. Cumulative particle size distributions under different inlet pressure are calculated based on the particle data

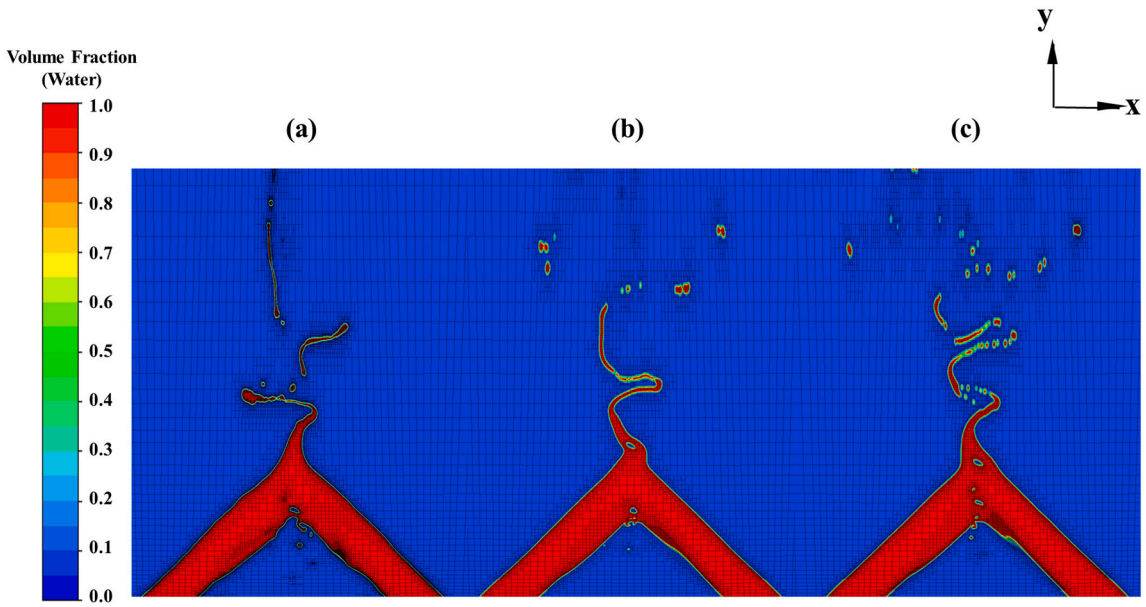

Fig. 9. Interfacial dynamics and numerical grids at x-y cut section view in mid-plane at 0.07 ms for: (a) $p = 5$ bar, $\overline{u}_j = 22.7$ m/s, $We = 477$, $Re = 1516$ (b) $p = 7$ bar, $\overline{u}_j = 27.6$ m/s, $We = 705$, $Re = 1844$ (c) $p = 10$ bar, $\overline{u}_j = 34.1$ m/s, $We = 1077$, $Re = 2278$. (a × b = 100 × 50 μm^2, 2φ = 90°).

recorded from the plane (Fig. 10). It reveals that the average particle size decreases with increasing pressure due to more intense flapping of liquid sheet at higher Weber number and higher Reynolds number, thus the liquid rim disintegrates more thoroughly, resulting in shorter and more unstable ligaments. The disintegration of liquid sheet is also referred to as the primary breakup. This process directly influences the disintegration of ligaments into droplets, which is also referred to as secondary breakup, so the unstable ligaments produced in the primary breakup undergo further disruption into droplets with smaller average size [44].

3.3.4. *Velocity profile analysis*

The velocity distribution at the central axis of two jets for different inlet pressures are shown in the Fig. 11. It is indicated that the absolute value of component velocity in the X direction reaches the lowest at the impingement point, due to the offset of the velocity vectors of two jets in opposite directions along the X-axis (see Fig. 11 (a)). The velocity gradient at the impingement point increases with the increasing inlet pressure of nozzle. The reason is that higher inlet pressure led to larger velocity component in the X direction, resulting in greater impact force generated, so the momentum of one jet decreases more sharply at the impingement point. It can be inferred that larger impact force is the major cause of more intense impact waves and more violent fluctuation of the liquid sheet as the inlet pressure of nozzle increases. The velocity component in the Y-axis increases as the pressure increases and has slight fluctuation near the impingement point due to the unequal longitudinal velocity of jets when colliding (see Fig. 11 (b)). As the velocity in the X direction cancels out after colliding of two jets, The velocity component in the Y-axis of jets directly influences the velocity of the liquid sheet. Therefore, the increase of velocity in the Y direction of liquid jets gives rise to the larger velocity and wider diffusion of the liquid sheet as the inlet pressure of nozzle increases.

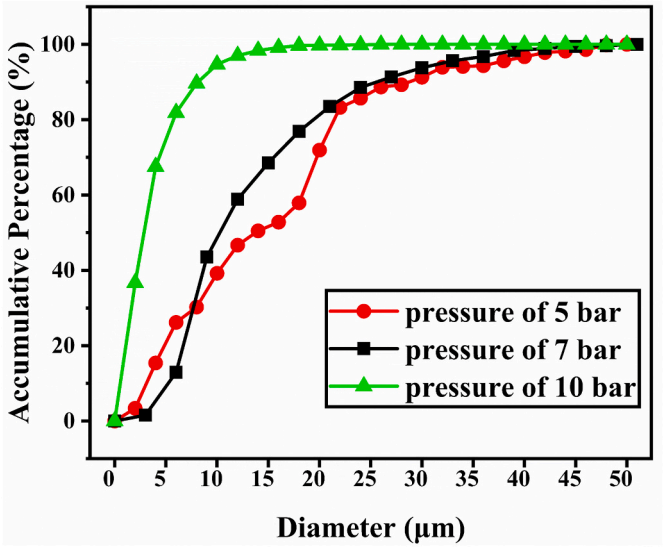

Fig. 10. Cumulative particle size distribution under different inlet pressure. (a × b = 100 × 50 μm^2, 2φ = 90°).

3.4. *Effect of impinging angle on atomization process*

To investigate the effect of impingement angle on atomization, the inlet pressure of nozzle was kept constant and the impingement angle is the only variable. The impingement angles of 60°and 90° have been chosen, while the inlet pressure was 7 bar. The parameters of model with different impingement angles were shown in Table 5.

3.4.1. *Liquid sheet pattern analysis*

Fig. 12 (a) and (b) show the velocity contours of inner zone of nozzle, nozzle exit and liquid sheet at 0.07 ms for the Case 2–1 and 2–2. It demonstrates that the impingement angle is of significant importance to the plume geometry and spray pattern.

When the impingement angle is less than 90°, a decrease in impingement angle leads to a wider diffusion range of liquid sheet and a reduction in spray angle and spray width along the z-axis, resulting in the elongation of liquid sheet (see Fig. 12 (b)). This is due to the larger velocity of the liquid sheet. As the impingement angle rises to 90°, increasing instability in impact waves and more violent oscillations of the liquid sheet indicate a stronger impact of two impinging jets. This significantly reduces the breakup length of liquid sheet.

The breakup pattern varies with different impingement angle. Fig. 12 (a) shows the impact wave pattern at the 90° impact angle [41]. Obvious impact waves occur on the surface of liquid sheet with short wavelength

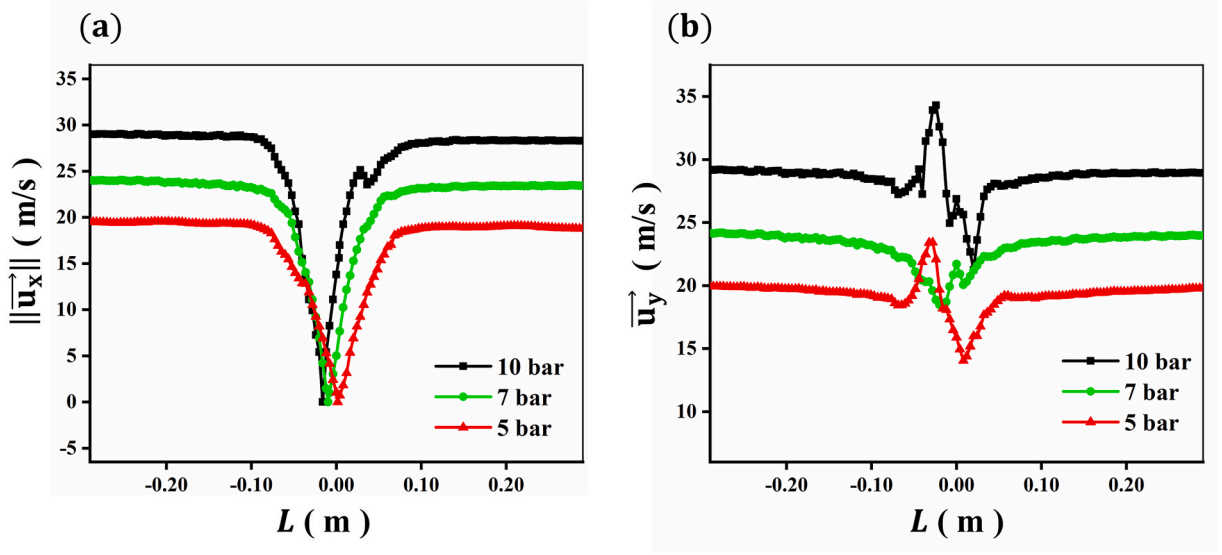

Fig. 11. Velocity distribution at the central axis of two jets with different inlet pressure: (a) absolute value of component in the X direction, and (b) component velocity in the Y direction.

Table 5
Parameters of model with different impingement angles.

Case	Impingement angle (°)	Nozzle size (μm^2)	Time (ms)	Inlet pressure (bar)	Mean jet velocity (m/s)	Weber number	Reynolds number
2–1	90	100 × 50	0.07	7	27.6	705	1844
2–2	60	100 × 50	0.07	7	29.2	746	1951

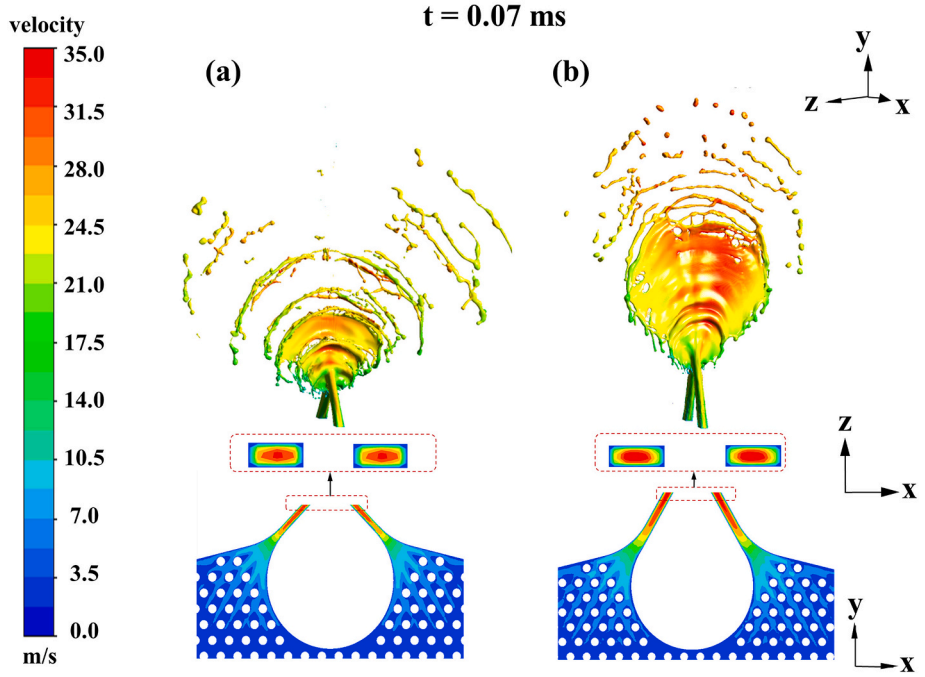

Fig. 12. Comparison of velocity distribution of the nozzle exit, central plane of nozzle vertical to nozzle exit and liquid sheet between different impingement angle: (a) 2φ = 90°, $\overline{u}_j$= 29.2 m/s, *We* = 705, *Re* = 1844 (b) 2φ = 60°, $\overline{u}_j$= 27.6 m/s, *We* = 746, *Re* = 1951. (a × b = 100 × 50 μm^2, *p* = 7 bar).

and large amplitude. At the impingement angle of 60°, the fluctuation of the liquid sheet is less obvious, and holes appear in the downstream of the liquid sheet. The hole expands to the rim and the liquid sheet breaks into ligaments, which is the unstable rim pattern as shown in Fig. 12 (b). Different impingement angles cause varying patterns of liquid sheet fragmentation, which can be mainly attributed to the differences in hydrodynamic fluctuations generated by the collision.

3.4.2. *Mesh adaption and interfacial dynamics*

As shown in Fig. 13 (a), fluctuations occur near the impact point at

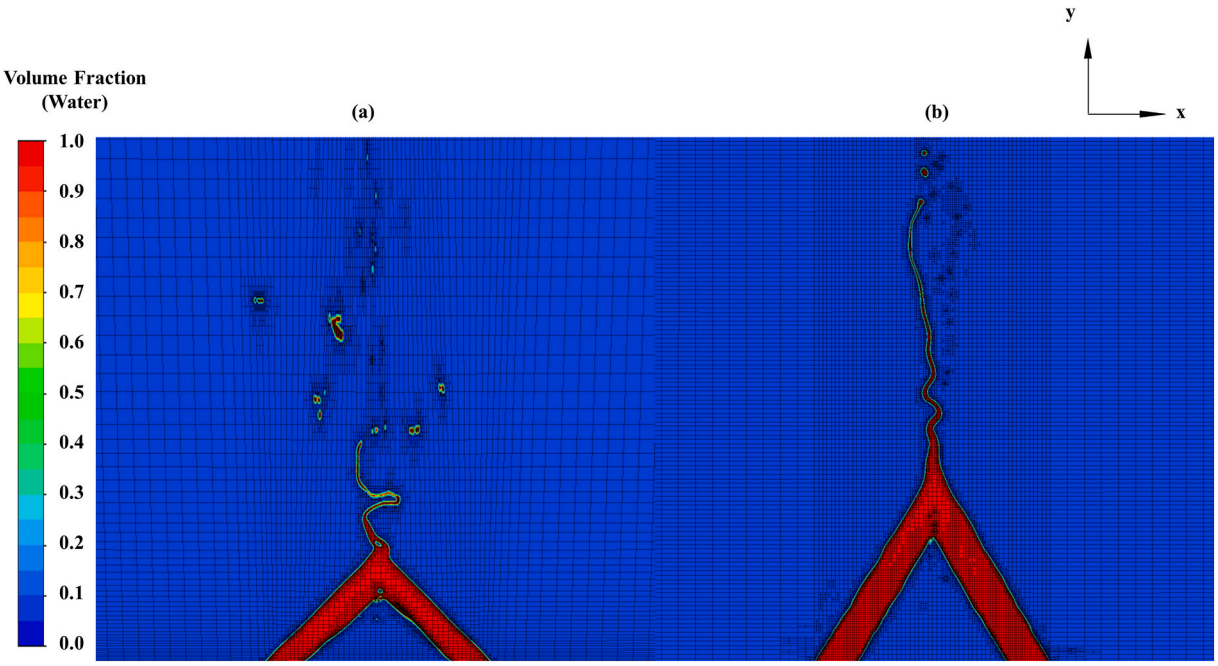

Fig. 13. Interfacial dynamics and numerical grids at x-y cut section view in mid-plane at 0.07 ms for: (a) $2\varphi = 90°$, $\overline{u}_j = 27.6$ m/s, $We = 705$, $Re = 1844$ (b) $2\varphi = 60°$, $\overline{u}_j = 29.2$ m/s, $We = 746$, $Re = 1951$ (a × b = 100 × 50 μm^2, $p = 7$ bar).

an impingement angle of 90°, which is the result of the hydrodynamic waves generated by the slamming collision. The amplitude of waves increases rapidly, causing the fluid liquid sheet to oscillate, and thus the liquid sheet breaks under fluctuating instability with short breakup length. When the impingement angle is 60°, the fluctuation near the impact point is insignificant, while obvious fluctuations occur in the downstream region because of the aerodynamic wave (see Fig. 13 (b)). The wave amplitude is small, so the liquid sheet surface fluctuates gently and the break-up length is long. Therefore, fluctuations of the liquid sheet have close relation with the impingement angles, and affect the liquid sheet fragmentation. When the impingement angle rises, the liquid sheet fluctuations are more intense, the liquid sheet instability intensifies and the breakup length decreases.

3.4.3. Particle size distribution analysis

Planes are created at 1.5 mm from the nozzle to record DPM particles which passed through the plane during flow time from 0.05 ms to 0.06 ms Fig. 14 shows that the average particle size declines as the impact angle rises. The mode of liquid sheet fragmentation plays a crucial role in particle size distribution. As mentioned before, the liquid sheet fluctuates more violently and the fragmentation is more complete at the impingement angle of 90°, hence the average particle size decreases significantly. At the impingement angle of 60°, the liquid sheet fluctuates mildly and the fragmentation degree is much smaller than that at the impingement angle of 90°. Arun Kumar has also noted the decrease of average particle size as the impingement angle rises by investigating the particle size distribution of jets impinging at angles of 50° and 80°, which is consistent with our results [38].

3.4.4. Velocity distribution analysis

The velocity distribution in the direction of X-axis and Y-axis at the central axis of jets with different impingement angles is shown in Fig. 15. When the impingement angle is 90°, although the mean jet velocity is smaller, the velocity in the X direction is larger which is proportional to the impingement angle, and the slope near the impingement point is steeper. It is indicated that the impact force produced from the impingement point is more violent, thus resulting in the rapid reduction in the momentum of one jet. It can be inferred that the larger velocity

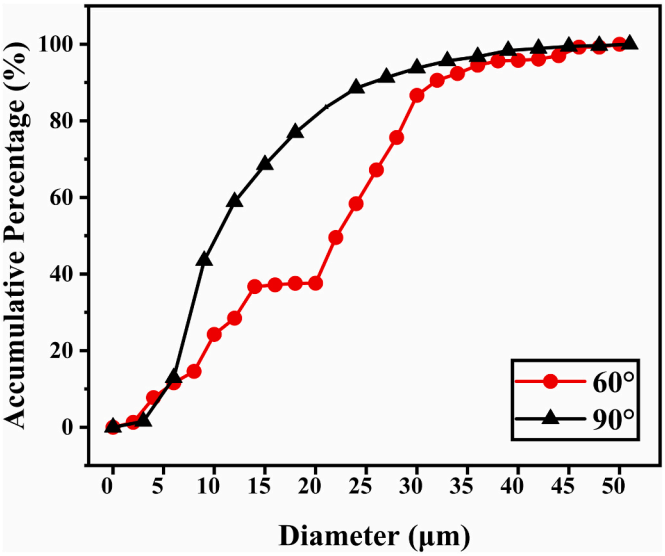

Fig. 14. Cumulative particle Size Distribution with different impingement angle. (a × b = 100 × 50 μm^2, p = 7 bar).

component in X direction is the direct factor which enhance the impact force generated, thus intensifying the amplitude and frequency of the impact wave at the impingement angle of 90°. Compared to that, the liquid sheet merely has slight fluctuation at the impingement angle of 60° because of the smaller component velocity in the direction of X-axis and less impact force generated. Meanwhile, the component velocity in the Y direction decreases as the impingement angle increases. The curve of component velocity in the Y direction decline slightly near the impingement point owing to the kinetic energy loss in the collision. The momentum of the liquid jets in the direction of Y-axis is transferred to the liquid sheet, and therefore the velocity and longitudinal diffusion of the liquid sheet at the impingement angle of the 60° is larger. Given the less violent fluctuation and larger velocity of the liquid sheet, the breakup length at the impingement angle of the 60° increases

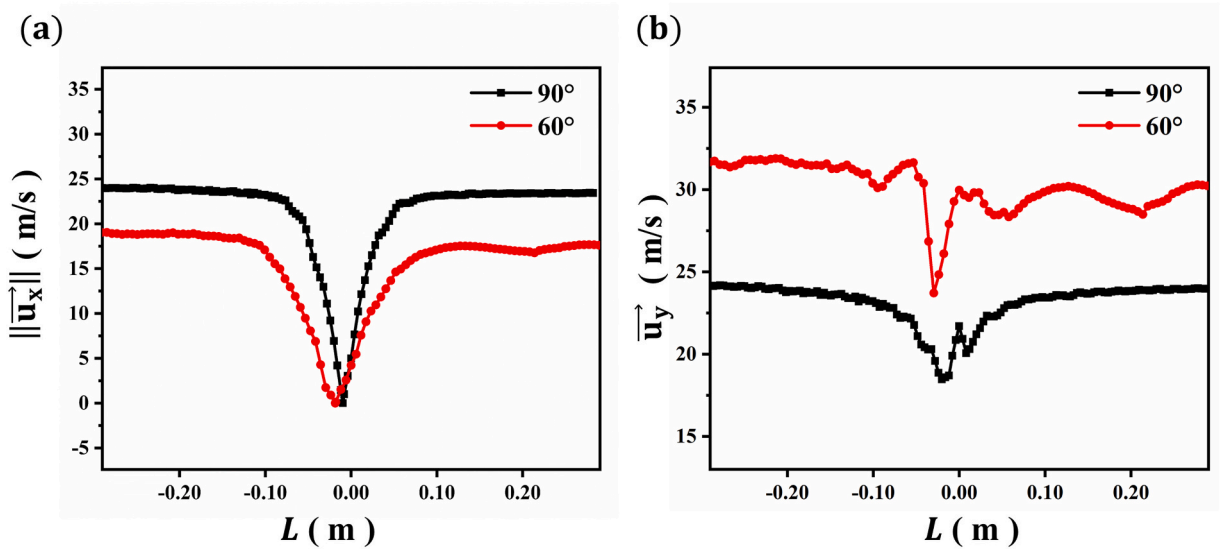

Fig. 15. Velocity distribution at the central axis of two jets with different impingement angle: (a) absolute value of component in the X direction, and (b) component velocity in the Y direction.

significantly.

4. Conclusions

This study developed a VOF-to-DPM model for the simulation of impinging jets atomization of soft mist inhalers. This method has successfully coupled the internal and external flow fields of the nozzle in the atomization process, so the effects of nozzle operating condition on the atomization characteristics can be taken into account. The plume geometry and the particle size distribution predicted by this model show overall agreement with experimental results. The numerical results show that impingement angle and velocity distribution of jet affected by the flow conditions inside the nozzle, have crucial effects on the atomization characteristics. The rise in the impingement angle and pressure at nozzle inlet leads to larger velocity component in the X direction of the liquid jet, resulting in greater impact force generated at the impingement point, which influences the fluctuation and breakup pattern of the liquid sheet directly, hence creating finer droplets. Moreover, the velocity component in the Y direction of the liquid jet determines the velocity and diffusion of the liquid sheet. Therefore, the x-component and y-component velocities the liquid jets have crucial effects on the breakup length of the liquid sheet simultaneously.

In future, it would be interesting to explore atomization dynamics through nozzles of even smaller size using higher grid resolution. The general mapping approach is suitable for analyzing dynamics of impinging jets through micron nozzles or nozzles with complex structures, which will lead to optimized design of nozzles with improved atomization performance.

Declaration of Interest Statement

We declare that we have no financial and personal relationships with other people or organizations that can inappropriately influence our work, there is no professional or other personal interest of any nature or kind in any product, service and/or company that could be constructed as influencing the position presented in, or the review of, the manuscript entitled.

Declaration of Competing Interest

None.

Acknowledgments

The authors are grateful for the research funds provided by the National Key Research and Development Project of China (2021YFB1715500). Financial supports from the National Natural Science Foundation of China (21978184) are also sincerely acknowledged.

References

[1] J.M. Borghardt, C. Kloft, A. Sharma, Inhaled therapy in respiratory disease: the complex interplay of pulmonary kinetic processes, Can. Respir. J. 2018 (2018) 2732017.
[2] D. Ganderton, General factors influencing drug delivery to the lung, Respir. Med. 91 (1997) 13–16.
[3] R. Dalby, M. Spallek, T. Voshaar, A review of the development of Respimat® soft mistTM inhaler, Int. J. Pharm. 283 (2004) 1–9.
[4] D.E. Geller, A.L. Coates, 18 - drug administration by inhalation in children, in: R. W. Wilmott, T.F. Boat, A. Bush, V. Chernick, R.R. Deterding, F. Ratjen (Eds.), Kendig & Chernick's Disorders of the Respiratory Tract in Children (Eighth Edition), W.B. Saunders, Philadelphia, 2012, pp. 284–298.
[5] V. Komalla, M. Haghi, Chapter 18 - Liposomes in the treatment of chronic respiratory conditions, in: K. Dua, P.M. Hansbro, R. Wadhwa, M. Haghi, L.G. Pont, K.A. Williams (Eds.), Targeting Chronic Inflammatory Lung Diseases Using Advanced Drug Delivery Systems, Academic Press, 2020, pp. 375–392.
[6] D. Hochrainer, H. Hölz, C. Kreher, L. Scaffidi, M. Spallek, H. Wachtel, Comparison of the aerosol velocity and spray duration of Respimat® soft mistTM inhaler and pressurized metered dose inhalers, J. Aerosol. Med. 18 (2005) 273–282.
[7] D.E. Geller, New liquid aerosol generation devices: systems that force pressurized liquids through nozzles, Respir. Care 47 (2002) 1392–1404 (discussion 1404-1395).
[8] R.N. Dalby, J. Eicher, B. Zierenberg, Development of Respimat(®) soft mistTM inhaler and its clinical utility in respiratory disorders, Med. Dev. (Auckl.) 4 (2011) 145–155.
[9] G. Taylor, Formation of thin flat sheets of water, in: Proceedings of the Royal Society of London Series A, Mathematical and Physical Sciences 259, 1960, pp. 1–17.
[10] M. Heidmann, R.J. Priem, J.C. Humphrey, A study of sprays formed by two impinging jets, in: National Advisory Committee for Aeronautics, 1957.
[11] Y. Tanasawa, S. Sasaki, N. Magai, The atomization of liquid by means of flat impingement, Technol. Rep. Tohoku Univ. 22 (1957).
[12] N.D. Dombrowski, P.C. Hooper, A study of the sprays formed by impinging jets in laminar and turbulent flow, J. Fluid Mech. 18 (1964) 392–400.
[13] J.C.P. Huang, The break-up of axisymmetric liquid sheets, J. Fluid Mech. 43 (1970) 305–319.
[14] E.A. Ibrahim, A.J. Przekwas, Impinging jets atomization, physics of fluids a, Fluid Dynam. 3 (1991) 2981–2987.
[15] R. Li, N. Ashgriz, Characteristics of liquid sheets formed by two impinging jets, Phys. Fluids 18 (2006), 087104.
[16] R.J. Santoro, I. Ryan, M. Harry, W.E. Anderson, Impact wave-based model of impinging jet atomization 16 (2006) 791–806.
[18] C. Liu, L. Zhou, P. Lei, Overview on numerical simulations of primary atomization, J. Rocket Propuls. 40 (2014) 10–17.

[19] K. Luo, S. Changxiao, Y. Yang, J. Fan, A mass conserving level set method for detailed numerical simulation of liquid atomization, J. Comput. Phys. 298 (2015).
[20] T. Himeno, C. Inoue, T. Watanabe, Study on free-surface flows in aerospace propulsion systems, Interdiscip. Inf. Sci. 17 (2011).
[21] D. Kim, O. Desjardins, M. Herrmann, P. Moin, The Primary Breakup of a Round Liquid Jet by a Coaxial Flow of Gas, 2007.
[22] M. Herrmann, A parallel Eulerian interface tracking/Lagrangian point particle multi-scale coupling procedure, J. Comput. Phys. 229 (2010) 745–759.
[23] M. Gorokhovski, M. Herrmann, Modeling primary atomization, Annu. Rev. Fluid Mech. 40 (2008) 343–366.
[24] X. Chen, V. Yang, S. Popinet, High-Fidelity simulations of impinging jet atomization, Atomiz. Sprays 23 (2013).
[25] G. Tomar, D. Fuster, S. Zaleski, S. Popinet, Multiscale simulations of primary atomization, Comp. Fluids - Comput. Fluids 39 (2010).
[26] D.-J. Ma, X.-D. Chen, P. Khare, V. Yang, Atomization patterns and breakup characteristics of liquid sheets formed by two impinging jets, in: 49th AIAA Aerospace Sciences Meeting including the New Horizons Forum and Aerospace Exposition, American Institute of Aeronautics and Astronautics, 2011.
[27] T. Ménard, S. Tanguy, A. Berlemont, Coupling level set/VOF/ghost fluid methods: validation and application to 3D simulation of the primary break-up of a liquid jet, Int. J. Multiphase Flow 33 (2007) 510–524.
[28] G. Zheng, W. Nie, S. Feng, G. Wu, Numerical simulation of the atomization process of a like-doublet impinging rocket injector, Procedia Eng. 99 (2015) 930–938.
[29] Q. Li, J. Ouyang, B. Yang, X. Li, Numerical simulation of gas-assisted injection molding using CLSVOF method, Appl. Math. Model. 36 (2012) 2262–2274.
[30] H. Wachtel, S. Kattenbeck, S. Dunne, B. Disse, The Respimat® development story: patient-centered innovation, pulmonary, Therapy 3 (2017) 19–30.
[31] R. Wang, P. Allmendinger, L. Zhu, A.J. Gröhn, K. Wegner, V. Frankevich, R. Zenobi, The role of nebulizer gas flow in Electrosonic spray ionization (ESSI), J. Am. Soc. Mass Spectrom. 22 (2011) 1234–1241.
[32] J.U. Brackbill, D.B. Kothe, C. Zemach, A continuum method for modeling surface tension, J. Comput. Phys. 100 (1992) 335–354.
[33] S. Morsi, A. Alexander, An investigation of particle trajectories in two-phase flow systems, J. Fluid Mech. 55 (1972) 193–208.
[34] M. Pai, I. Bermejo-Moreno, O. Desjardins, H. Pitsch, Role of Weber number in the primary breakup of liquid jets in crossflow, 2009, p. LK.009.
[35] S. Jung, S. Hoath, G. Martin, I. Hutchings, Atomization patterns produced by the oblique collision of two Newtonian liquid jets, Phys. Fluids 22 (2010).
[36] K. Jung, T. Khil, Y. Yoon, T.-S. Roh, The Breakup Characteristics of Liquid Sheet Formed by Like-Doublet Injectors, 2002.
[37] A. Mansour, N. Chigier, Disintegration of liquid sheets, physics of fluids A, Fluid Dynam. 2 (1990) 706–719.
[38] A.K. Balasubramanian, V. Kumar, P. Nakod, J. Schütze, A. Rajan, Multiscale modelling of a doublet injector using hybrid VOF-DPM method, in: AIAA Scitech 2020 Forum, American Institute of Aeronautics and Astronautics, 2020.
[39] T. Inamura, M. Shirota, Effect of velocity profile of impinging jets on sheet characteristics formed by impingement of two round liquid jets, Int. J. Multiphase Flow 60 (2014).
[40] X. Chen, D.-J. Ma, V. Yang, Dynamics and Stability of Impinging Jets, Annual Conference on Liquid Atomization and Spray System, San Antonian, TX, 2012.
[41] X. Chen, P. Khare, V. Yang, Atomization patterns and breakup characteristics of liquid sheets formed by two impinging jets, in: 49th AIAA Aerospace Sciences Meeting, 2011, pp. 2011–2097.
[42] B.E. Rapp, Chapter 23 - plateau-Rayleigh instability, in: B.E. Rapp (Ed.), Microfluidics: Modelling, Mechanics and Mathematics, Elsevier, Oxford, 2017, pp. 467–477.
[43] T.J. Tharakan, K. Ramamurthi, M. Balakrishnan, Nonlinear breakup of thin liquid sheets, Acta Mech. 156 (2002) 29–46.
[44] A. Zandian, S. William, F. Hussain, Three-dimensional liquid sheet breakup: vorticity dynamics, in: 54th AIAA Aerospace Sciences Meeting, 2012.
[45] G. Bailardi, M. Negri, H. Ciezki, Several aspects of the atomization behavior of various Newtonian fluids with a like-on-like impinging jet injector. ILASS-Europe 2010, 23rd Annual Conference on Liquid Atomization and Spray Systems, 2010.